ACS NANO
Cite This: ACS Nano 2019, 13, 8926–8935
www.acsnano.org

ARTICLE

High-Mobility, Wet-Transferred Graphene Grown by Chemical Vapor Deposition

Domenico De Fazio,[†,#] David G. Purdie,[†,#] Anna K. Ott,[†] Philipp Braeuninger-Weimer,[‡] Timofiy Khodkov,[§] Stijn Goossens,[§] Takashi Taniguchi,[⊥] Kenji Watanabe,[⊥] Patrizia Livreri,[∥] Frank H. L. Koppens,[§] Stephan Hofmann,[‡] Ilya Goykhman,[†] Andrea C. Ferrari,[†] and Antonio Lombardo*[,†]

[†]Cambridge Graphene Centre, University of Cambridge, Cambridge CB3 0FA, U.K.
[‡]Department of Engineering, University of Cambridge, Cambridge CB3 0FA, U.K.
[§]ICFO-Institut de Ciencies Fotoniques, The Barcelona Institute of Science and Technology, 08860 Castelldefels (Barcelona), Spain
[⊥]National Institute for Materials Science, 1-1 Namiki, Tsukuba 305-0044, Japan
[∥]Universitá degli Studi di Palermo, 90128 Palermo, Italy

ABSTRACT: **We report high room-temperature mobility in single-layer graphene grown by chemical vapor deposition (CVD) after wet transfer on SiO_2 and hexagonal boron nitride (hBN) encapsulation. By removing contaminations, trapped at the interfaces between single-crystal graphene and hBN, we achieve mobilities up to ∼70000 $cm^2 V^{-1} s^{-1}$ at room temperature and ∼120 000 $cm^2 V^{-1} s^{-1}$ at 9K. These are more than twice those of previous wet-transferred graphene and comparable to samples prepared by dry transfer. We also investigate the combined approach of thermal annealing and encapsulation in polycrystalline graphene, achieving room-temperature mobilities of ∼30 000 $cm^2 V^{-1} s^{-1}$. These results show that, with appropriate encapsulation and cleaning, room-temperature mobilities well above 10 000 $cm^2 V^{-1} s^{-1}$ can be obtained in samples grown by CVD and transferred using a conventional, easily scalable PMMA-based wet approach.**

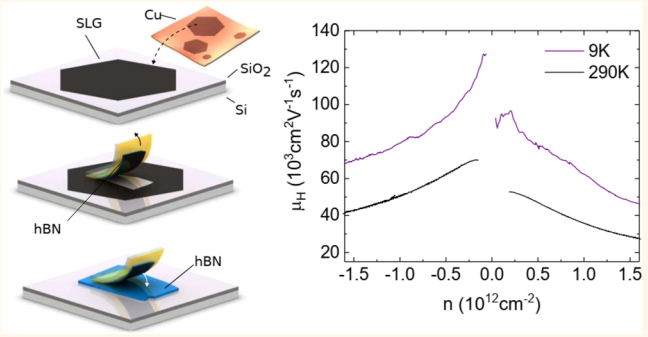

KEYWORDS: *graphene, CVD, transfer, heterostructures, charge carrier mobility*

In a crystal lattice, the charge carrier mobility (μ) is the proportionality constant between the carriers' drift velocity and the electric field that causes their motion.[1] Charge carrier mobility is an important figure of merit for materials to be used in electronic devices such as field effect transistors (FETs), as it determines the transit time of charge carriers across the device channel and therefore its cutoff frequency.[1,2] Also, conductivity is proportional to mobility,[1] and therefore, higher mobility leads to higher currents, which can charge capacitances faster and hence determine better frequency response.[2] μ is also a crucial factor for optical devices, as parameters such as insertion loss and extinction ratio depend on the scattering time,[3] which (according to the Kubo model) is proportional to the carrier mobility.[3,4]

Charge carriers in single-layer graphene (SLG) can reach room-temperature (RT) μ > 200 000 $cm^2 V^{-1} s^{-1}$ at technologically relevant carrier densities $n \approx 10^{12}$ cm^{-2}, corresponding to a sheet conductivity $\sigma \approx 30$ mS, with $\sigma = e\mu n$ and e the elementary charge 1.6×10^{-19}C [1], limited by electron−phonon interactions.[5,6] High μ > 10 000 $cm^2 V^{-1} s^{-1}$ at such carrier densities is essential for (opto)electronic devices,[3] such as microwave transistors,[7] photodetectors,[8] THz detectors,[9] and optical modulators.[3,10] RT μ > 100 000 $cm^2 V^{-1} s^{-1}$ can be achieved in micromechanically cleaved (MC) samples, either suspended[11−14] or encapsulated in hexagonal boron nitride (hBN).[15−17] This is twice that of InSb[15,18,19] and InAs[15,18] at n up to ∼4.5×10^{12} cm^{-2} (corresponding to a Fermi level $E_F \approx 270$ meV).[5,15] Integration of SLG in a foundry requires scalable production and fabrication methods, to meet the requirements for 300 mm wafers.[3] Chemical vapor deposition (CVD) allows production of SLG with lateral sizes up to hundreds of meters.[20,21] A Cu foil is widely used as a substrate due to its low carbon solubility (∼0.005 carbon weight % at 1084 °C)[23] and its catalytic role during growth.[24,25] Polycrystalline continuous films[26,27] or isolated single crys-

Received: April 4, 2019
Accepted: July 19, 2019
Published: July 19, 2019

DOI: 10.1021/acsnano.9b02621
ACS Nano 2019, 13, 8926–8935

tals[28−31] can be grown by tuning parameters such as partial pressures,[32] temperature T,[33] or substrate roughness.[34,35]

In order to be integrated into devices, SLG needs then to be removed from Cu and placed onto the target substrate. Several transfer methods have been developed, classified as either "wet" or "dry". We consider "wet" all techniques whereby the SLG surface gets in contact with liquids, such as water,[36] solvents,[26,27] or other chemicals used to remove the substrate or any supporting layer[36] at any step of the transfer process. Wet transfer exploits a sacrificial layer (either a polymer[26,27,37−41] or a thermal release tape[26]) as support for SLG while the substrate is removed by chemical etching,[26,27,37] electrochemical delamination,[38] or selective interface etching.[42] Wet transfer is simple and easily scalable;[26] however it introduces polymer residuals or defects that typically reduce the SLG quality, resulting in undesired doping[39] or low μ (<3000 cm^2 V^{-1} s^{-1}[20]) and is therefore considered unsuitable for the production of high-mobility (>10 000 cm^2 V^{-1} s^{-1}) samples.[22] The highest μ at RT reported to date in wet-transferred CVD SLG is ∼20 000 cm^2 V^{-1} s^{-1},[39,41] achieved by placing SLG onto mechanically exfoliated hBN.[39−41] This is almost 1 order of magnitude lower than the state of the art in MC samples transferred by stamping.[17] Wet transfer was also used to CVD-hBN/CVD SLG stacks where both hBN and SLG were grown by CVD.[48] However, μ reported in ref 48 is just ∼3000 cm^2 V^{-1} s^{-1}, comparable to that of SLG on SiO$_2$,[21] thus with no improvement brought about by the more complex fabrication approach.

Dry transfer consists in peeling SLG off the substrate without any chemical etching or electrochemical delamination. This exploits the van der Waals interaction between SLG and hBN.[43,44] An hBN flake placed on a polymeric stamp is used to pick up SLG.[43,44] The hBN-SLG stack is subsequently stamped onto a second hBN layer, achieving full encapsulation (*i.e.*, the entire SLG area is enclosed between two hBN layers), so that SLG is never in contact with any liquid.[43,44] μ up to ∼3 × 10^6 cm^2 V^{-1} s^{-1} at 1.8 K was reported for dry transferred, encapsulated, CVD-grown SLG,[43,44] comparable to MC SLG encapsulated in hBN.[15−17] Dry transfer requires Cu oxidation below the SLG surface,[43,44] to weaken the SLG interaction with Cu.[43] However, Cu oxidation can be a time-consuming process (a few days are required for oxidation of Cu underneath SLG islands of a few hundred μm width at ambient conditions[45]), and its speed depends on the SLG coverage of the Cu foil, as SLG slows down the oxidation process.[46]

We reported a method to clean interfaces in heterostructures consisting of MC SLG and hBN,[17] achieving atomically clean interfaces and RT μ up to ∼150 000 cm^2 V^{-1} s^{-1} even in samples intentionally contaminated with polymers and solvents.[17] Here we apply the same approach to CVD-grown single crystal (SC) SLG domains (lateral size ∼500 μm) wet transferred on Si +SiO$_2$. We achieve μ up to ∼70 000 cm^2 V^{-1} s^{-1} at RT and ∼120 000 cm^2 V^{-1} s^{-1} at 9 K, with ballistic transport over ∼600 nm at 9 K. To the best of our knowledge, this is the highest μ reported thus far in wet-transferred, CVD-grown SLG. We also apply the same approach to polycrystalline SLG (poly-SLG) with average grain size of a few μm^2, achieving RT $\mu \approx$ 7000 cm^2 V^{-1} s^{-1}. By then annealing in Ar/H$_2$ at 600 °C we get RT μ of up to ∼30 000 cm^2 V^{-1} s^{-1}. Thus, by combining encapsulation and interface cleaning, both SC and poly CVD-grown SLG have RT $\mu \gg$ 10 000 cm^2 V^{-1} s^{-1} even after exposure to contaminants such as etchants, polymers, and solvents. Therefore, scalable processing methods, such as polymer-based wet transfer, can be used for fabrication of (opto)electronic devices achieving the μ required for them to surpass existing technologies.[3]

RESULTS AND DISCUSSION

SLG single crystals are grown on Cu (see Figure 1), following the procedure discussed in the Methods section. Electron

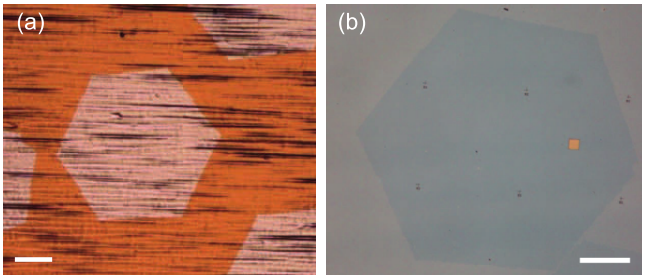

Figure 1. (a) Optical microscope image of hexagonal-shaped SC-SLG grown on Cu by CVD. Contrast for imaging SC is enhanced by heating the sample in air at 250 °C on a hot plate for 1 min to promote the oxidation of Cu. (b) Optical image of SC-SLG wet transferred on SiO$_2$/Si with patterned lithography markers. Scale bars: 100 μm.

diffraction on multiple spots reveals the same crystal orientation across the hexagonal SLG domain with ∼500 μm lateral size.[49]

SLG crystals are then transferred on Si+285 nm SiO$_2$ using a wet method.[26,27,36] A poly(methyl methacrylate) (PMMA) support layer is spin coated at the SLG surface. The samples are then placed in a solution of ammonium persulfate (APS) and deionized (DI) water, whereby Cu is chemically etched.[26,27,36] The PMMA/SLG stack is then moved to a beaker with DI water to remove APS residuals and lifted with the target SiO$_2$/Si substrate. After drying, PMMA is removed in acetone, leaving SLG on SiO$_2$/Si, Figure 1b. We then encapsulate SLG in hBN. hBN bulk crystals are grown as for ref 50. These are mechanically exfoliated on Si+285 nm SiO$_2$ to be used for SLG encapsulation. Flakes of lateral size >100 μm are identified and selected by inspecting the SiO$_2$/Si surface using a combination of bright and dark field optical microscopy, Raman spectroscopy, and atomic force microscopy (AFM). For the top hBN we use flakes with thickness $t_{hBN} \approx$ 2−300 nm. For the bottom hBN, flakes with t_{hBN} > 10 nm are chosen, as thinner ones do not screen roughness and charged impurities of the underlying SiO$_2$.[17,51]

The encapsulation of SLG in hBN typically results in blisters containing trapped adsorbates and contaminants,[52] which must be avoided, as they locally degrade transport.[52] Reference 53 showed how to remove contamination blisters by a hot pick-up technique. This uses T above the glass transition, T_g, of the polymer stamp during encapsulation, allowing the interfaces of two materials to be brought together in a directional, conformal manner.[53] We modified this approach by using polycarbonate (PC) stamps at T = 180 °C, achieving fast (>10 μm/s) removal of contaminants in fully encapsulated hBN/SLG/hBN heterostructures.[17] This results in atomically flat interfaces even on samples intentionally contaminated with polymers and solvents, achieving in all cases RT μ > 150 000 cm^2 V^{-1} s^{-1}.[17] As for ref 17, here we use a transfer stamp consisting of a PC film on a polydimethylsiloxane (PDMS) block for mechanical support, placed on a glass slide attached to a micromanipulator, enabling fine (∼1 μm) spatial control in x, y, and z. T is set using a heated stage. The process is depicted in Figure 2. It begins by positioning the stamp above a hBN flake, then lowering it into

DOI: 10.1021/acsnano.9b02621
ACS Nano 2019, 13, 8926−8935

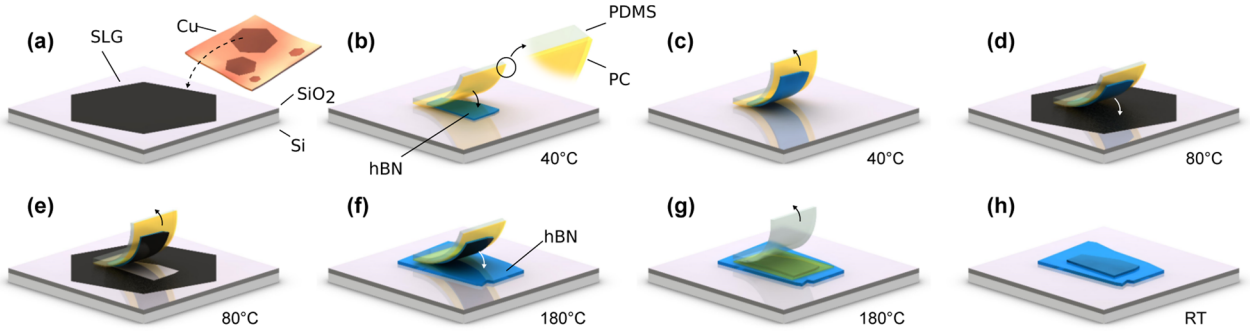

Figure 2. Schematics of the transfer process to encapsulate SLG in hBN. (a) SLG (black hexagon) is wet-transferred from Cu to Si+285 nm SiO_2. In parallel, (b, c) top hBN (light blue) is picked up with a PC/PDMS stamp (yellow and white). (d, e) SLG is then picked up with the top hBN from Si/SiO_2 at 80 °C and (f, g) hot-released at 180 °C on the bottom hBN, leaving the PC/hBN/SLG/hBN stack on the substrate. (h) PC is removed by chloroform.

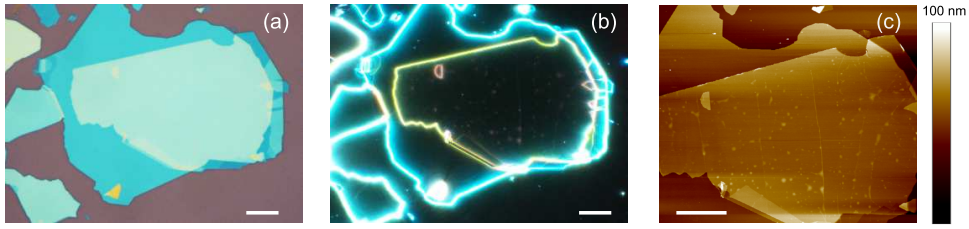

Figure 3. (a) Bright field, (b) dark field, and (c) AFM images of SC-SLG encapsulated in hBN. Scale bars: 10 μm.

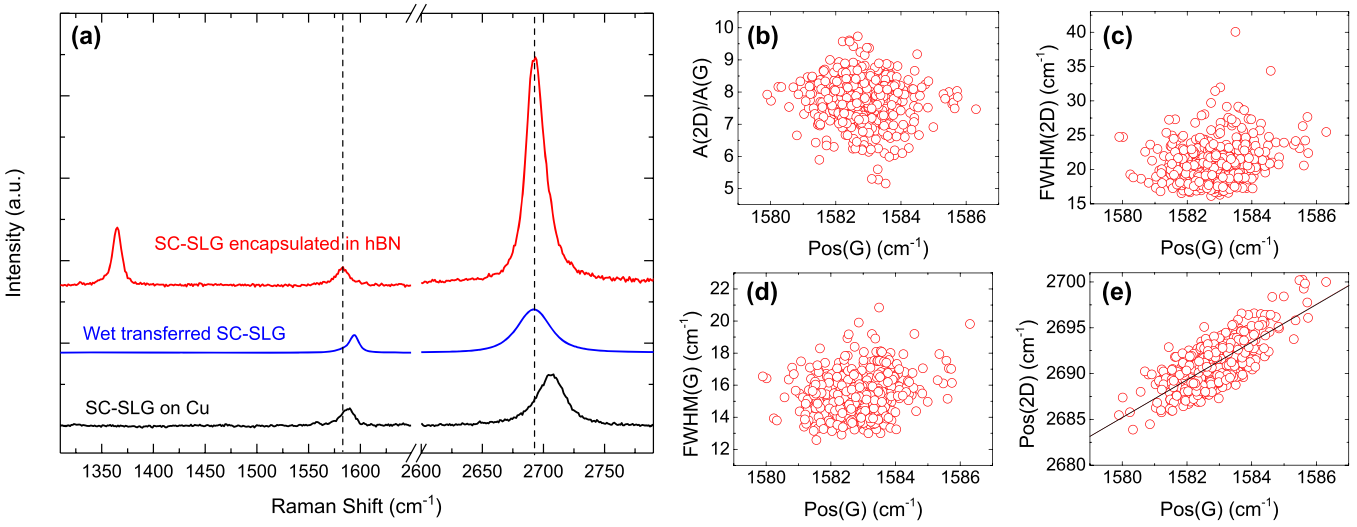

Figure 4. (a) Raman spectra measured at an excitation wavelength of 514 nm of as-grown SC-SLG on Cu (black curve), wet transferred on SiO_2 (blue curve), and encapsulated in hBN (red curve). In the spectrum on Cu, the PL of Cu has been subtracted. Plots of (b) $A(2D)/A(G)$, (c) FWHM(2D), (d) FWHM(G), and (e) Pos(2D) as a function of Pos(G) and mapped across a 20 μm × 30 μm region in an SC-SLG encapsulated in hBN.

contact, with the stage T set to 40 °C. As the stamp is withdrawn, the hBN adheres to the PC surface and is delaminated from SiO_2, Figure 2b,c. The picked-up hBN is then positioned above the (wet-transferred) SLG on SiO_2 and brought into contact at 80 °C. We then wait ∼5 min to promote adhesion between hBN and SLG, after which the stamp is lifted, picking up the SLG portion in contact with hBN, Figure 2d,e. The final step consists in bringing the top hBN/SLG into contact with the bottom hBN at 180 °C, with the stamp tilted to ensure that contact occurs first on one side, then conformally advancing across the substrate, Figure 2f. At 180 °C, withdrawing the stamp releases the PC onto the substrate, Figure 2g. PC is then dissolved by placing the sample in chloroform, Figure 2h. Figure 3a,b are bright and dark field images of the final hBN/SLG/hBN stack. Scans by AFM, Figure 3c, reveal that some blisters are present. They tend to aggregate in specific areas, mostly along vertical lines, which we attribute to residual wrinkles from wet transfer.

The SLG quality is monitored at each step of the fabrication process by Raman spectroscopy. Raman measurements are performed with a Renishaw InVia spectrometer equipped with a 100× objective, 2400 l/mm grating at 514 nm. The power on the sample is less than ∼1 mW to avoid any heating and damage. Figure 4a plots representative spectra of a SC-SLG on Cu (black), after transfer on SiO_2/Si (blue), and encapsulated in hBN (red). The SLG spectrum on Cu is shown after subtraction of the Cu photoluminescence (PL).[54] This has a 2D peak with a

DOI: 10.1021/acsnano.9b02621
ACS Nano 2019, 13, 8926−8935

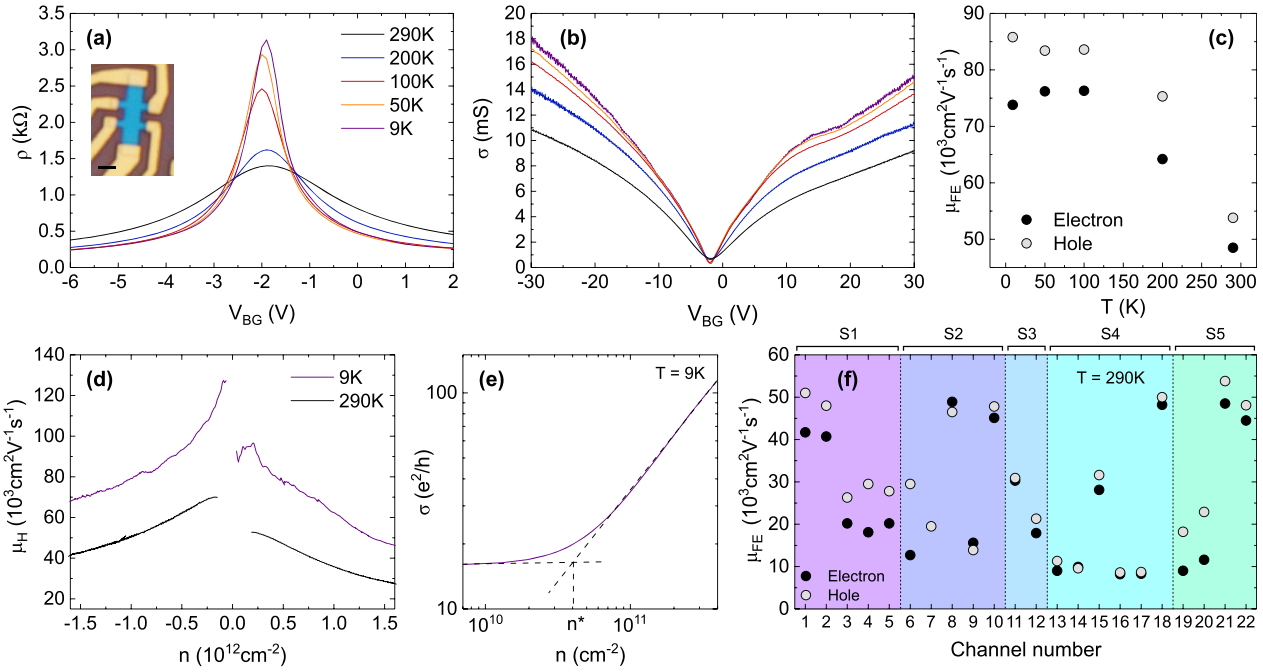

Figure 5. (a) Resistivity as a function of gate voltage between 9 and 290 K. Inset: Optical image of the device, with a scale bar of 1.5 μm. (b) Electrical conductivity as a function of gate voltage with temperature color-code matching that of (a). (c) Field effect mobility μ_{FE} as a function of T for holes and electrons. (d) Density-dependent Hall mobility μ_H from the Drude model $\mu = \sigma/ne$ at 9 and 290 K. (e) Low-temperature (9 K) conductivity as a function of carrier density close to the charge neutrality point on logarithmic axes and corresponding extraction of disorder-induced charge inhomogeneity n^*. (f) μ_{FE} for 22 Hall bars fabricated on five encapsulated SC-SLG heterostructures. Each shaded region corresponds to one of the five different samples (S1−S5), while black (gray) dots refer to electron (hole) mobilities in each channel.

single Lorentzian shape and with a full width at half-maximum (FWHM)(2D) ≈ 27 cm^{-1}, a signature of SLG.[55] The position of the G peak, Pos(G), is ∼1588 cm^{-1}, with FWHM(G) ≈ 14 cm^{-1}. The 2D peak position, Pos(2D), is ∼2706 cm^{-1}, while the 2D to G peak intensity and area ratios, I(2D)/I(G) and A(2D)/A(G), are ∼3 and ∼5.5. No D peak is observed, indicating negligible defects.[56,57] After wet transfer on SiO_2/Si, the 2D peak retains its single-Lorentzian line shape with FWHM(2D) ≈ 30 cm^{-1}. The D peak is still negligible, indicating that no significant defects are induced by wet transfer. Pos(G) is ∼1594 cm^{-1}, FWHM(G) ≈ 11 cm^{-1}, Pos(2D) ≈ 2692 cm^{-1}, and I(2D)/I(G) and A(2D)/A(G) are ∼2.5 and ∼6.8, indicating a doping of <200 meV.[58,59]

After pick up and encapsulation, we perform Raman mapping over an area of ∼20 μm × 30 μm, using the same measurement conditions. A representative spectrum is shown in red in Figure 4a. This comprises both the SLG signatures and the hBN E_{2g} peak at ∼1364 cm^{-1}, with an FWHM of ∼9.5 cm^{-1}, as expected for bulk hBN.[60−62] The hBN E_{2g} peak is a combination of top and bottom hBN and may overlap a small D peak.

Figure 4b−e plot Raman data extracted from mapping: A(2D)/A(G), FWHM(2D), FWHM(G), and Pos(2D) as a function of Pos(G). Pos(G) depends on both doping[58,59] and strain.[63] This implies that local variations in strain and doping manifest as a spread in Pos(G), which in our sample varies from 1580 to 1586 cm^{-1}. The samples have narrow 2D peaks with mean FWHM(2D) ≈ 20 ± 3 cm^{-1}. Figure 4b−d plot A(2D)/A(G) and FWHM(G) as a function of Pos(G), indicating small variations of both doping and strain within the SLG layer. The mean A(2D)/A(G) is ∼7.8 ± 0.7, while the mean FWHM(G) is ∼15.4 ± 1.2 cm^{-1}. The high A(2D)/A(G) is an indication of intrinsic samples,[58] when combined with FWHM(G) ≈ 15 cm^{-1}, as well as Pos(G) ≈ 1583 cm^{-1} and Pos(2D) ≈ 2693 cm^{-1}.[58]

The rate of change of Pos(2D) and Pos(G) with strain is ruled by the Grüneisen parameters (γ),[63] which relate the relative change in the peak positions in response to strain(ϵ), *i.e.*, $\gamma = [\omega - \omega_0]/[2\epsilon\omega_0]$, where ω is the frequency of Raman peaks at finite strain and ω_0 the frequency at zero strain.[63] For biaxial strain the Grüneisen parameters for G and 2D peak are respectively $\gamma_G \approx 1.8$ and $\gamma_{2D} \approx 2.6$, resulting in ΔPos(2D)/ΔPos(G) ≈ 2.5.[63−65] In the case of uniaxial strain $\gamma_G \approx 1.8$;[63] however extraction of γ_{2D} is not straightforward, as uniaxial strain shifts the relative position of the SLG Dirac cones,[63,65] which in turn affects the 2D peak, as this involves intervalley scattering.[56,63] Reference 63 experimentally derived an upper bound $\gamma_{2D} \approx 3.55$ and theoretically calculated $\gamma_{2D} \approx 2.7$, consistent with experimentally reported ΔPos(2D)/ΔPos(G) ≈ 2−3.[63,66,67] Biaxial strain can be differentiated from uniaxial from the absence of G and 2D peak splitting with increasing strain;[56] however at low (≲0.5%) strain the splitting cannot be resolved.[63,66] Figure 4e shows the correlation between Pos(2D) and Pos(G). A linear fit gives a slope ΔPos(2D)/ΔPos(G) ≈ 2.07. The presence (or coexistence) of biaxial strain cannot be ruled out. For uniaxial(biaxial) strain, Pos(G) shifts by ΔPos(G)/$\Delta\epsilon$ ≈ 23(60)cm^{-1}/%.[63,65,66] For intrinsic SLG (E_F < 100 meV), the unstrained, undoped Pos(G) is ∼1581.5 cm^{-1}.[55,68] In Figure 4d the mean Pos(G) is 1582.8 cm^{-1}, which would lead to uniaxial(biaxial) strain $\epsilon \approx 0.05\%(0.02\%)$.[63,65,66] The scattering of A(2D)/A(G) within the mapped area indicates small (≪100 meV) variation of doping.

We then process our samples into Hall bars, in order to perform four-terminal electrical transport as discussed in the Methods. Figure 5a plots the resistivity of encapsulated CVD SLG as a function of back gate voltage, V_{BG}. An optical image of

DOI: 10.1021/acsnano.9b02621
ACS Nano 2019, 13, 8926−8935

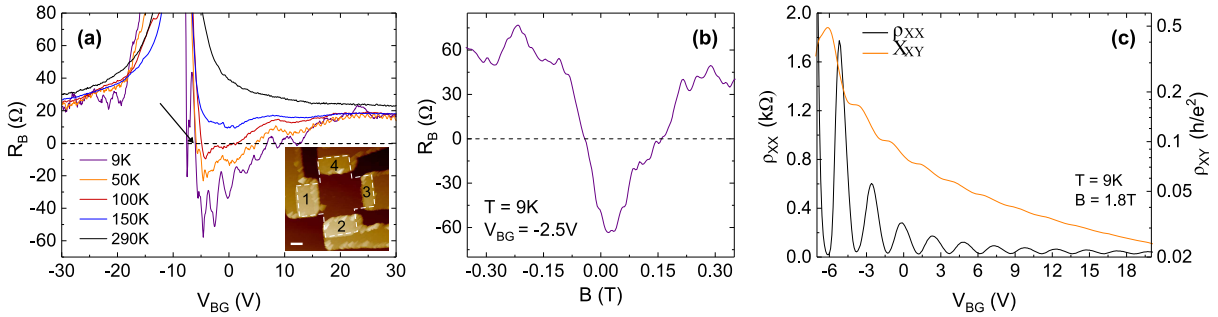

Figure 6. (a) Bend resistance of a Hall cross with arm width 640 nm as a function of V_{BG} for T ranging from 9 to 290 K. The negative resistance below 100 K for positive V_{BG} indicates that carriers travel ballistically from contacts 1 to 3. The arrow indicates $R_B = 0\ \Omega$ at approximately 100 K, *i.e.*, the transition from diffusive to ballistic transport at which $l_m \approx 640$ nm. Inset: AFM scan of the Hall cross sample with numbered contacts (scale bar: ~200 nm). (b) Bend resistance as a function of magnetic field, at $V_{BG} = -2.5$ V and $T = 9$ K. (c) Longitudinal resistivity ρ_{XX} (black curve) and transversal resistivity ρ_{XY} (orange curve) as a function of V_{BG} at 9 K and magnetic field $B = 1.8$ T.

one of the Hall bars is in the inset. The corresponding conductivity is shown in Figure 5b. We extract the field effect mobility $\mu_{FE} = C_{ox}^{-1}(d\sigma/dV_{BG})$ by performing a linear fit to the conductivity close to the charge neutrality point (CNP),[69] where C_{ox} is the gate capacitance per unit area. This is calculated as $\sim 1.1 \times 10^{-4}$ F/m^2, assuming a parallel plate capacitor where the bottom hBN is in series with the 285 nm SiO_2 layer.[17] The bottom hBN thickness is ~15 nm for the sample in Figure 5a. We assume a dielectric constant for hBN $\epsilon \approx 3$, considering that values between 2 and 4 are usually reported.[70] Our C_{ox} is orders of magnitude smaller than the quantum capacitance of SLG,[71] which is therefore neglected. This yields $\mu_{FE} \approx 49\,000$ cm^2 V^{-1} s^{-1} and 54 000 cm^2 V^{-1} s^{-1} for electrons and holes at 290 K. μ_{FE} as a function of T in Figure 5c reaches ~86 000 cm^2 V^{-1} s^{-1} for holes at 9 K. In order to extract μ as a function of n, we investigate transport in the presence of an out-of-plane magnetic field B (Hall effect).[1] To distinguish μ calculated from the Hall effect from that estimated from the slope of the conductivity, we indicate the first as μ_H.[1] Assuming a Drude model of conductivity, $\mu_H = \sigma/ne$,[1] where n is extracted by measuring the Hall voltage with $B = 0.5$ T. μ_H in Figure 5d reaches ~70 000 cm^2 V^{-1} s^{-1}, close to the CNP, while it is >30 000 cm^2 V^{-1} s^{-1} for n up to $\sim 1.5 \times 10^{12}$ cm^{-2}. At 9 K μ_H is >120 000 cm^2 V^{-1} s^{-1}.

Such values are consistent with those reported in CVD-grown SLG encapsulated in hBN using dry techniques.[43,44] For example, ref 43 measured $\mu_{FE} \approx$ 110 000–350 000 cm^2 V^{-1} s^{-1} at 1.6 K in Hall bars made with CVD SLG encapsulated by dry transfer in hBN. Reference 40 combined wet transfer of CVD-grown large (up to 250 μm wide) SLG onto hBN with thermal annealing, achieving $\mu \approx 45\,000$ cm^2 V^{-1} s^{-1} at $T = 1.6$ K, which is 2.5 lower than our μ at $T = 9$ K (120 000 cm^2 V^{-1} s^{-1}).[47]

Figure 5a shows that our SLG is nearly intrinsic, since the resistivity peak occurs close to zero gate voltage, at $V_{CNP} = -1.8$ V, indicating moderate $n \approx 1.2 \times 10^{11}$ cm^{-2} at $V_{BG} = 0$V, in agreement with the Raman analysis. Furthermore, the resistivity peak is narrow, with FWHM ~1 V at 9 K. This places an upper bound on the disorder-induced charge inhomogeneity, n^*, with narrower peaks corresponding to lower disorder.[11,52,72] $n^* < 10^{11}$ cm^{-2} is typically associated with either suspended[72] or dry encapsulated samples.[17,43] We extract n^* for our sample as for refs 12 and 72, Figure 5e, and get $\sim 4 \times 10^{10}$ cm^{-2}, 1 order of magnitude higher than clean MC samples.[17] In order to investigate the μ variation, we fabricate 22 Hall bars from five encapsulated SC-SLG. The distribution of μ_{FE} at RT in Figure 5f ranges from a minimum ~10 000 cm^2 V^{-1} s^{-1} up to ~55 000 cm^2 V^{-1} s^{-1}.

Bend resistance measurements as a function of T are typically used to probe ballistic transport in SLG,[15−17,43] whereby current is injected around a bend while measuring the voltage. In SLG the carrier mean free path l_m is related to conductivity:[73]

$$l_m = \frac{h}{2e^2}\sigma\sqrt{\frac{1}{\pi n}} \quad (1)$$

where h is the Planck constant. l_m can be extracted from Figure 5a. It varies from ~0.6 μm at 290 K up to ~1 μm at 9 K. For such l_m we expect ballistic transport.[16] We therefore fabricate a Hall cross with arm width $W = 640$ nm to perform bend resistance measurements as a function of T.[15,16,44]

An AFM scan of the Hall cross is in the inset of Figure 6a. A constant current $I_{1,2}$ is passed between contacts 1 and 2, and the voltage between contacts 3 (V_3) and 4 (V_4) is measured, from which $R_B = (V_4 - V_3)/I_{1,2}$ is extracted. In the diffusive regime, where $l_m < W$, a positive R_B is measured, related to the sheet resistance *via* the Van der Pauw formula:[74] $\rho = (\pi/\ln 2)R_B$. Alternatively, if $l_m \geq W$, carriers injected at contact 1 follow ballistic trajectories to contact 3, resulting in $R_B < 0$. R_B as a function of T is shown in Figure 6b. Below 100 K, R_B becomes negative for positive V_{BG}, indicating $l_m \geq 640$ nm. At the transition from the diffusive to ballistic $R_B = 0$ and $l_m \approx W$, from which μ may be estimated rearranging eq 1 by substituting $l_m = W$, to give[16]

$$\mu \approx \frac{2e}{h}W\sqrt{\frac{\pi}{n_{th}}} \quad (2)$$

where n_{th} is the carrier concentration at which $R_B = 0$. At 9 K, $R_B = 0$ occurs at $V_{BG} = -5.8$ V, as shown by the arrow in Figure 6a, corresponding to $\mu \approx 129\,000$ cm^2 V^{-1} s^{-1}, in agreement with the peak μ_H from Figure 5d. Further confirmation of ballistic transport is achieved by applying an out-of-plane B, which results in the bending of electrons from their straight-line trajectories, deflecting them away from contact 3, and switching R_B from negative to positive, Figure 6b. Magnetotransport at $B = 1.8$ T and 9 K, Figure 6c, shows resolved Landau levels, consistent with refs 40 and 43, proving the high electronic quality of our samples.

For all our samples $l_m \lesssim 1$ μm at 9 K, even in Hall bars with channel widths > 3 μm. This is supported by the fact that Hall crosses with width $W = 1$ μm exhibit no negative bend resistance at any T. Our maximum $l_m \approx 1$ μm is lower than dry transferred

DOI: 10.1021/acsnano.9b02621
ACS Nano 2019, 13, 8926−8935

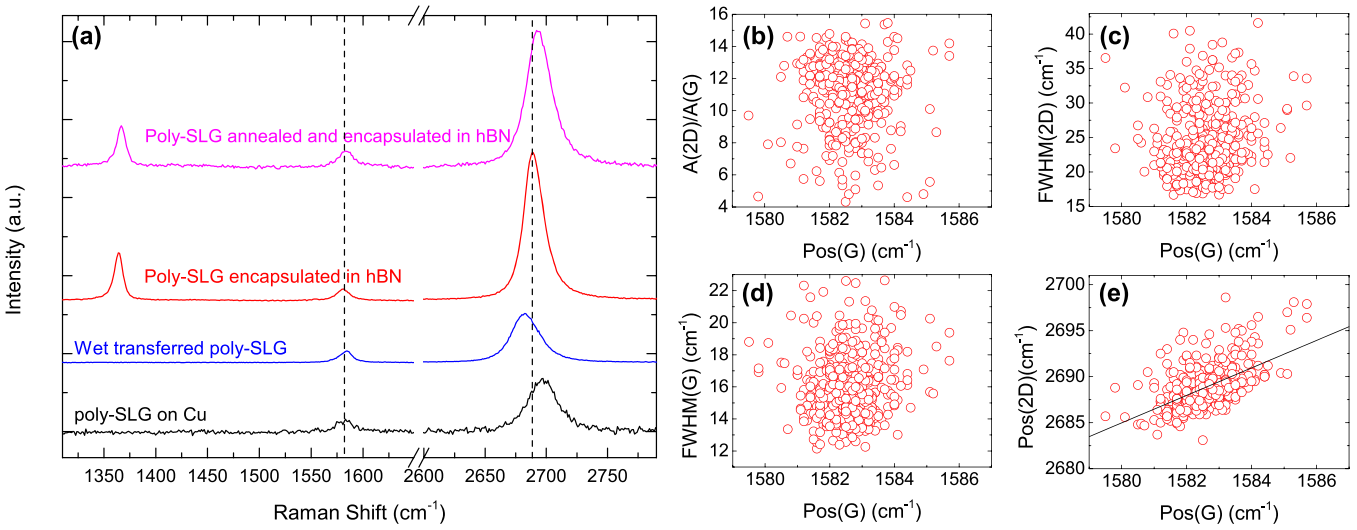

Figure 7. (a) Raman spectra measured at an excitation wavelength of 514 nm of as-grown poly-SLG on Cu (black curve), wet transferred on SiO_2 (blue curve), encapsulated in hBN (red curve), and annealed at 600 °C in Ar/H_2 and encapsulated in hBN (magenta curve). In the spectrum on Cu, the PL of Cu has been subtracted. Plots of (b) $A(2D)/A(G)$, (c) FWHM(2D), (d) FWHM(G), and (e) Pos(2D) as a function of Pos(G) and mapped across an 18 μm × 23 μm region in a poly-SLG encapsulated in hBN.

samples, in which l_m typically exceeds the sample dimensions at low T,[15,44] resulting in edge scattering limited conductivity. Indeed, the highest reported l_m in the literature are >10 μm,[15,44] over an order of magnitude larger than here. However, we note that l_m is not a limiting factor at RT, where μ is limited by electron−phonon scattering.[5,6,75]

In order to investigate the effect of grain boundaries on μ, we study μ_{FE} of poly-SLG (see Methods), CVD-grown, encapsulated in hBN by using the same approach. Due to the small domain size, multiple crystal orientations are present within the same Hall bar. SLG is wet transferred onto Si+285 nm SiO_2 and then encapsulated in hBN, following the same procedure as above, but with T = 180 °C in the pick-up step, as higher T is required to pick up poly-SLG from SiO_2.

The Raman spectra at each stage of the transfer process are shown in Figure 7. Compared to SC-SLG, the Raman parameters are more scattered; for example, the variation of $A(2D)/A(G)$ and Pos(G) is twice that of SC-SLG, indicating inhomogeneous doping. The mean $I(2D)/I(G)$ and $A(2D)/A(G)$ ratio are indeed ∼7.2 ± 2.1 and ∼11.1 ± 4.1, respectively, which indicate a mean doping of ∼100 ± 100 meV. Pos(G) in unstrained graphene with such low doping is ∼1581.6 cm^{-1}.[67] In our samples, however, the mean Pos(G) is ∼1582.6 ± −1.9 cm^{-1}, indicating the presence of uniaxial (biaxial) strain between $\epsilon \approx 0.02\%$ (0.05%) and $\epsilon \approx 0.03\%$ (0.09%).[63,65,66] The slope of ΔPos(2D)/ΔPos(G) in Figure 7f is ∼1.5 lower than in SC-SLG, due to the inhomogeneous distribution of doping and strain in these samples.

The resistivity as a function of V_{BG} is shown in Figure 8. By performing a linear fit to the conductivity close to CNP at $V_{BG} \approx$ 4 V, we get $\mu_{FE} = C_{ox}^{-1}(d\sigma/dV_{BG}) \approx 7000$ cm^2 V^{-1} s^{-1} and 5000 cm^2 V^{-1} s^{-1} for electrons and holes, respectively, at 290 K. These values are 1 order of magnitude lower compared to SC-SLG, as expected from the presence of grain boundaries. The shoulder on the left-hand side of the resistivity as a function of V_{BG} at $V_{BG} \approx -8$ V suggests the presence of an additional CNP in the SLG channel, indicating inhomogeneous doping,[76] in good agreement with the Raman analysis.

As μ in poly-SLG is significantly lower that SC-SLG, we investigate the combined effect of thermal annealing and

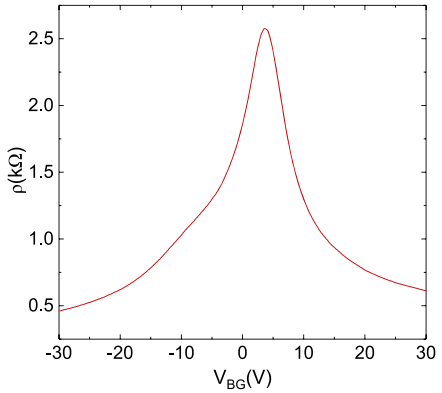

Figure 8. Electrical resistivity ρ measured at T = 290 K as a function of V_{BG} for a poly-SLG sample encapsulated in hBN and shaped in a Hall bar geometry.

encapsulation in poly-SLG. To do so, we first exfoliate hBN onto Si+285 nm SiO_2. Poly-SLG is then transferred to Si+285 nm SiO_2 using the polymer-based wet transfer detailed above.[26,27,36] This results in SLG partially on SiO_2 and partially on exfoliated hBN. The samples are then annealed at 600 °C in Ar/H_2 (40/40 sccm).

Spatially resolved Raman spectra are acquired before and after annealing, both on SLG on SiO_2 and on hBN. The annealing sharpens FWHM(2D) from a mean ∼27 to ∼23 cm^{-1} after annealing, Figure 9a. This suggests that annealing makes the sample more homogeneous in terms of doping/strain by aggregating adsorbates/contaminants in blisters as shown in Figure 9b. The annealed SLG is then encapsulated by depositing a second hBN using a polymer stamp following ref 53. Samples are then shaped into Hall bars and contacted using Ni/Pd electrodes (30/40 nm). Figure 9c plots the resistance as a function of gate. Figure 9d shows μ_{FE} in annealed and encapsulated poly-SLG, indicating a peak $\mu_{FE} \approx 30\,000$ cm^2 V^{-1} s^{-1}, showing that annealing improves μ_{FE} by a factor ∼5. We note that this is among the highest RT μ_{FE} claimed for poly-SLG to date.

DOI: 10.1021/acsnano.9b02621
ACS Nano 2019, 13, 8926−8935

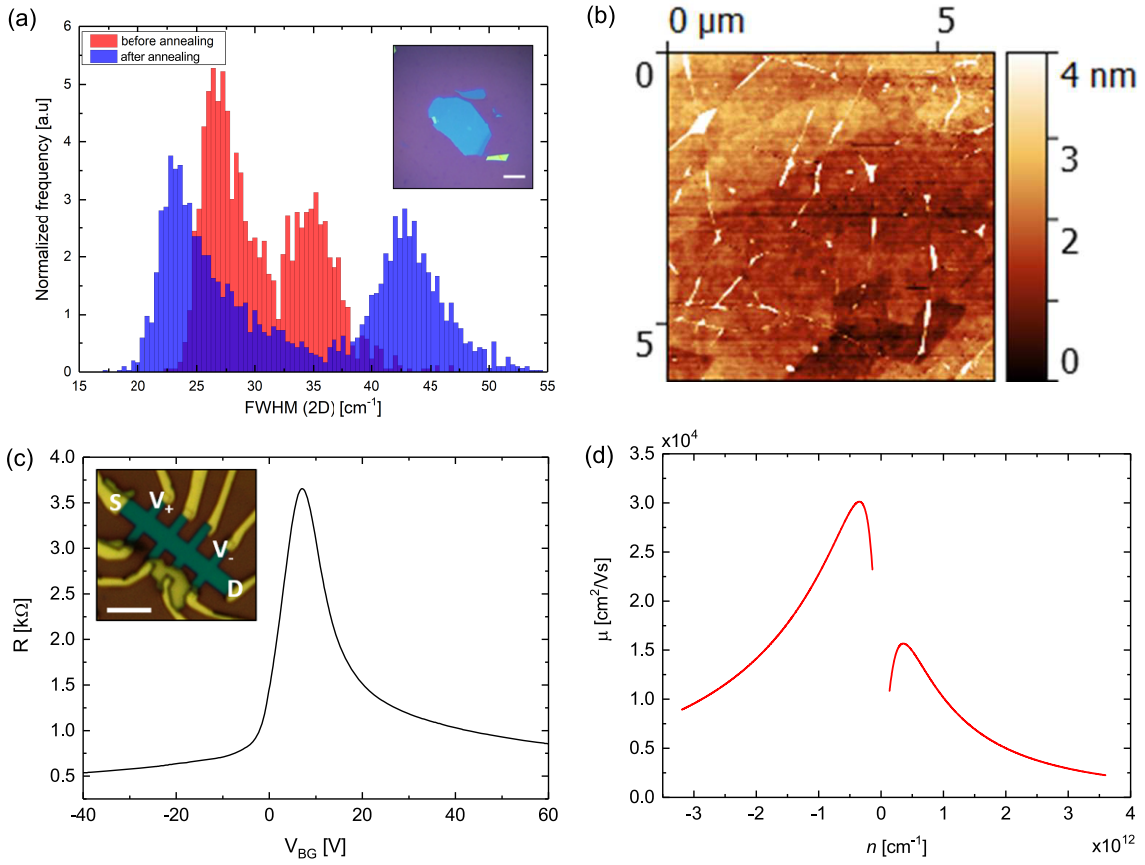

Figure 9. (a) Statistical distribution of FWHM(2D) acquired from Raman spectra measured on a poly-SLG on hBN (blue curve) before and (red curve) after annealing in Ar/H_2 at 600 °C. Spatially resolved Raman spectra are acquired by mapping poly-SLG layers partially on SiO_2 and partially encapsulated in hBN. The inset shows the sample mapped. Scale bar: 10 μm. (b) AFM image of poly-SLG on hBN after annealing. (c) Four-terminal resistance of annealed and encapsulated poly-SLG as a function of V_{BG}. The inset is an optical image of the device. Scale bar: 5 μm. The bias is applied between the (S) source and drain (D) electrodes, and the voltage drop along the sample is sensed between V_+ and V_-. (d) μ_{FE} as a function of n, extracted by assuming a Drude model for the conductivity.

CONCLUSIONS

We reported high mobility in CVD-grown, single-crystal SLG placed on Si+SiO_2 using wet transfer and subsequently encapsulated in hBN. By cleaning interfaces between SLG and hBN at ~180 °C, we achieved mobilities up to up ~70 000 cm^2 V^{-1} s^{-1} at RT and >120 000 cm^2 V^{-1} s^{-1} at 9 K, comparable to values achieved *via* dry transfer. The samples show ballistic transport over ~600 nm at 9 K. This confirms that encapsulation in hBN and interface cleaning enable high mobility even after conventional polymer-based wet transfer techniques. We also investigated the combined effect of annealing and encapsulation in polycrystalline SLG, achieving RT mobilities up to ~30 000 cm^2 V^{-1} s^{-1}. Our results show that easy and scalable processes such as wet transfer, so far considered to induce irreversible degradation in SLG,[43,44] can be used for the assembly of high-performance devices where high mobility (>10 000 cm^2 V^{-1} s^{-1}) is essential, provided that a suitable cleaning method is applied.

METHODS

Growth. SLG single crystals are grown on 25 μm thick Alfa Aesar, 99.8% purity Cu foil, Figure 1a. As for ref 49, before growth the Cu foil is floated on the surface of a 30% hydrogen peroxide (H_2O_2) solution at 100 °C for 5 min to oxidize the back side. This treatment favors the growth of single crystals due to oxygen-enabled scavenging of carbon impurities trapped in the Cu top surface and bulk, which would otherwise act as nucleation sites during the growth.[49] Growth is then performed in an Aixtron Black Magic Pro, 4 in. cold wall plasma enhanced CVD (PECVD) system with a base pressure of ~0.05 mbar. The foil is initially placed in the furnace and heated to ~1065 °C in a Ar environment (200 sccm) at 100 °C/min. Once the growth T is reached, the Cu foil is annealed keeping T constant in Ar (200 sccm) for 30 min. Carbon deposition is done in an Ar/H_2 environment (250/26 sccm) using 9 sccm CH_4, 0.1% diluted in Ar, for 45 min. Samples are then cooled in 250 sccm Ar to RT. The crystallinity of the as-grown SLG is confirmed *via* transmission electron microscopy.[49]

Poly-SLG is grown on 35 μm Cu, following ref 27. The substrate is annealed in 20 sccm H_2 up to 1000 °C for 30 min. Then, 5 sccm of CH_4 is added for the growth to take place for an additional 30 min. The sample is then cooled under vacuum (~1.3 mbar) to RT and unloaded from the chamber.

Device Fabrication. To form contacts, we follow ref 15. After defining the shape of the desired Hall bar using a hard mask,[17] patterned by e-beam lithography, we remove the unmasked part by reactive ion etching using a plasma formed from a mix of tetrafluoromethane (CF_4) and oxygen (O_2) (ratio 4:1) under a 20 W forward radio frequency power. SLG is then contacted at its edges[15] by depositing metal leads *via* e-beam evaporation of 5/70 nm Cr/Au.

AUTHOR INFORMATION

Corresponding Author

*E-mail: al515@cam.ac.uk.

ORCID

Philipp Braeuninger-Weimer: 0000-0001-8677-1647

Frank H. L. Koppens: 0000-0001-9764-6120

DOI: 10.1021/acsnano.9b02621
ACS Nano 2019, 13, 8926−8935

Stephan Hofmann: 0000-0001-6375-1459
Andrea C. Ferrari: 0000-0003-0907-9993
Antonio Lombardo: 0000-0003-3088-6458

Author Contributions

#D.D.F. and D.G.P. contributed equally.

Notes

The authors declare no competing financial interest.

ACKNOWLEDGMENTS

We acknowledge funding from the EU Graphene Flagship, ERC Grant Hetero2D, EPSRC Grants EP/K016636/1, EP/K01711X/1, EP/K017144/1, EP/N010345/1, and EP/L016087/1, Wolfson College Cambridge, the Elemental Strategy Initiative conducted by MEXT, and JSPS KAKENHI Grant JP15K21722.

REFERENCES

(1) Sze, S. M.; Ng, K. K. *Physics of Semiconductor Devices*; John Wiley & Sons: Hoboken, NJ, 2006.
(2) Schroder, D.K. *Semiconductor Material and Device Characterization*; John Wiley & Sons: Hoboken, NJ, 2006.
(3) Romagnoli, M.; Sorianello, V.; Midrio, M.; Koppens, F. H. L.; Huyghebaert, C.; Neumaier, D.; Galli, P.; Templ, W.; D'Errico, A.; Ferrari, A. C. Graphene-Based Integrated Photonics for Next-Generation Datacom and Telecom. *Nat. Rev. Mater.* **2018**, *3*, 392−414.
(4) Gusynin, V. P.; Sharapov, S. G.; Carbotte, J. P. Magneto-optical conductivity in graphene. *J. Phys.: Condens. Matter* **2007**, *19*, 026222.
(5) Chen, J. H.; Jang, C.; Xiao, S. D.; Ishigami, M.; Fuhrer, M. S. Intrinsic and Extrinsic Performance Limits of Graphene Devices on SiO_2. *Nat. Nanotechnol.* **2008**, *3*, 206−209.
(6) Park, C.-H.; Bonini, N.; Sohier, T.; Samsonidze, G.; Kozinsky, B.; Calandra, M.; Mauri, F.; Marzari, N. Electron−Phonon Interactions and the Intrinsic Electrical Resistivity of Graphene. *Nano Lett.* **2014**, *14*, 1113−1119.
(7) Lin, Y. M.; Dimitrakopoulos, C.; Jenkins, K. A.; Farmer, D. B.; Chiu, H. Y.; Grill, A.; Avouris, P. 100-GHz Transistors from Wafer-Scale Epitaxial Graphene. *Science* **2010**, *327*, 662−662.
(8) Koppens, F. H. L.; Mueller, T.; Avouris, P.; Ferrari, A. C.; Vitiello, M. S.; Polini, M. Photodetectors Based on Graphene, Other Two-Dimensional Materials and Hybrid Systems. *Nat. Nanotechnol.* **2014**, *9*, 780−793.
(9) Vicarelli, L.; Vitiello, M. S.; Coquillat, D.; Lombardo, A.; Ferrari, A. C.; Knap, W.; Polini, M.; Pellegrini, V.; Tredicucci, A. Graphene Field-Effect Transistors as Room-Temperature Terahertz Detectors. *Nat. Mater.* **2012**, *11*, 865−871.
(10) Sorianello, V.; Midrio, M.; Contestabile, G.; Asselberghs, I.; Van Campenhout, J.; Huyghebaert, C.; Goykhman, I.; Ott, A. K.; Ferrari, A. C.; Romagnoli, M. Graphene-Silicon Phase Modulators with Gigahertz Bandwidth. *Nat. Photonics* **2018**, *12*, 40−44.
(11) Bolotin, K. I.; Sikes, K. J.; Jiang, Z.; Klima, M.; Fudenberg, G.; Hone, J.; Kim, P.; Stormer, H. L. Ultrahigh Electron Mobility in Suspended Graphene. *Solid State Commun.* **2008**, *146*, 351−355.
(12) Du, X.; Skachko, I.; Barker, A.; Andrei, E. Y. Approaching Ballistic Transport in Suspended Graphene. *Nat. Nanotechnol.* **2008**, *3*, 491−495.
(13) Bolotin, K. I.; Ghahari, F.; Shulman, M. D.; Stormer, H. L.; Kim, P. Observation of the Fractional Quantum Hall Effect in Graphene. *Nature* **2009**, *462*, 196−199.
(14) Mayorov, A. S.; Elias, D. C.; Mukhin, I. S.; Morozov, S. V.; Ponomarenko, L. A.; Novoselov, K. S.; Geim, A. K.; Gorbachev, R. V. How Close Can One Approach the Dirac Point in Graphene Experimentally? *Nano Lett.* **2012**, *12*, 4629−4634.
(15) Wang, L.; Meric, I.; Huang, P. Y.; Gao, Q.; Gao, Y.; Tran, H.; Taniguchi, T.; Watanabe, K.; Campos, L. M.; Muller, D. A.; Guo, J.; Kim, P.; Hone, J.; Shepard, K. L.; Dean, C. R. One-Dimensional Electrical Contact to a Two-Dimensional Material. *Science* **2013**, *342*, 614−617.
(16) Mayorov, A. S.; Gorbachev, R. V.; Morozov, S. V.; Britnell, L.; Jalil, R.; Ponomarenko, L. A.; Blake, P.; Novoselov, K. S.; Watanabe, K.; Taniguchi, T.; Geim, A. K. Micrometer-Scale Ballistic Transport in Encapsulated Graphene at Room Temperature. *Nano Lett.* **2011**, *11*, 2396−2399.
(17) Purdie, D. G.; Pugno, N. M.; Taniguchi, T.; Watanabe, K.; Ferrari, A. C.; Lombardo, A. Cleaning Interfaces in Layered Materials Heterostructures. *Nat. Commun.* **2018**, *9*, 5387.
(18) Bennett, B. R.; Magno, R.; Boos, J. B.; Kruppa, W.; Ancona, M. G. Antimonide-Based Compound Semiconductors for Electronic Devices: A Review. *Solid-State Electron.* **2005**, *49*, 1875−1895.
(19) Orr, J. M. S.; Gilbertson, A. M.; Fearn, M.; Croad, O. W.; Storey, C. J.; Buckle, L.; Emeny, M. T.; Buckle, P. D.; Ashley, T. Electronic Transport in Modulation-Doped InSb Quantum Well Heterostructures. *Phys. Rev. B: Condens. Matter Mater. Phys.* **2008**, *77*, 165334.
(20) Kobayashi, T.; Bando, M.; Kimura, N.; Shimizu, K.; Kadono, K.; Umezu, N.; Miyahara, K.; Hayazaki, S.; Nagai, S.; Mizuguchi, Y.; Murakami, Y.; Hobara, D. Production of a 100m-Long High-Quality Graphene Transparent Conductive Film by Roll-to-Roll Chemical Vapor Deposition and Transfer Process. *Appl. Phys. Lett.* **2013**, *102*, 023112.
(21) Li, X. S.; Cai, W. W.; An, J. H.; Kim, S.; Nah, J.; Yang, D. X.; Piner, R.; Velamakanni, A.; Jung, I.; Tutuc, E.; Banerjee, S. K.; Colombo, L.; Ruoff, R. S. Large-Area Synthesis of High-Quality and Uniform Graphene Films on Copper Foils. *Science* **2009**, *324*, 1312−1314.
(22) Lin, L.; Deng, B.; Sun, J. Y.; Peng, H. L.; Liu, Z. F. Bridging the Gap between Reality and Ideal in Chemical Vapor Deposition Growth of Graphene. *Chem. Rev.* **2018**, *118*, 9281−9343.
(23) López, G. A.; Mittemeijer, E. J. The Solubility of C in Solid Cu. *Scr. Mater.* **2004**, *51*, 1−5.
(24) Li, X.; Zhu, Y.; Cai, W.; Borysiak, M.; Han, B.; Chen, D.; Piner, R. D.; Colombo, L.; Ruoff, R. S. Transfer of Large-Area Graphene Films for High-Performance Transparent Conductive Electrodes. *Nano Lett.* **2009**, *9*, 4359−4363.
(25) Mattevi, C.; Kim, H.; Chhowalla, M. A Review of Chemical Vapour Deposition of Graphene on Copper. *J. Mater. Chem.* **2011**, *21*, 3324−3334.
(26) Bae, S.; Kim, H.; Lee, Y.; Xu, X. F.; Park, J. S.; Zheng, Y.; Balakrishnan, J.; Lei, T.; Kim, H. R.; Song, Y. I.; Kim, Y. J.; Kim, K. S.; Ozyilmaz, B.; Ahn, J. H.; Hong, B. H.; Iijima, S. Roll-to-Roll Production of 30-Inch Graphene Films for Transparent Electrodes. *Nat. Nanotechnol.* **2010**, *5*, 574−578.
(27) Li, X. S.; Cai, W. W.; An, J. H.; Kim, S.; Nah, J.; Yang, D. X.; Piner, R.; Velamakanni, A.; Jung, I.; Tutuc, E.; Banerjee, S. K.; Colombo, L.; Ruoff, R. S. Large-Area Synthesis of High-Quality and Uniform Graphene Films on Copper Foils. *Science* **2009**, *324*, 1312−1314.
(28) Yu, Q.; Jauregui, L. A.; Wu, W.; Colby, R.; Tian, J.; Su, Z.; Cao, H.; Liu, Z.; Pandey, D.; Wei, D.; Chung, T. F.; Peng, P.; Guisinger, N. P.; Stach, E. A.; Bao, J.; Pei, S.-S.; Chen, Y. P. Control and Characterization of Individual Grains and Grain Boundaries in Graphene Grown by Chemical Vapour Deposition. *Nat. Mater.* **2011**, *10*, 443−449.
(29) Li, X.; Magnuson, C. W.; Venugopal, A.; Tromp, R. M.; Hannon, J. B.; Vogel, E. M.; Colombo, L.; Ruoff, R. S. Large-Area Graphene Single Crystals Grown by Low-Pressure Chemical Vapor Deposition of Methane on Copper. *J. Am. Chem. Soc.* **2011**, *133*, 2816−2819.
(30) Miseikis, V.; Bianco, F.; David, J.; Gemmi, M.; Pellegrini, V.; Romagnoli, M.; Coletti, C. Deterministic Patterned Growth of High-Mobility Large-Crystal Graphene: A Path Towards Wafer Scale Integration. *2D Mater.* **2017**, *4*, 021004.
(31) Gao, L.; Ren, W.; Xu, H.; Jin, L.; Wang, Z.; Ma, T.; Ma, L.-P.; Zhang, Z.; Fu, Q.; Peng, L.-M.; Bao, X.; Cheng, H.-M. Repeated Growth and Bubbling Transfer of Graphene with Millimetre-Size Single-Crystal Grains Using Platinum. *Nat. Commun.* **2012**, *3*, 699.
(32) Vlassiouk, I.; Regmi, M.; Fulvio, P.; Dai, S.; Datskos, P.; Eres, G.; Smirnov, S. Role of Hydrogen in Chemical Vapor Deposition Growth of Large Single-Crystal Graphene. *ACS Nano* **2011**, *5*, 6069−6076.

DOI: 10.1021/acsnano.9b02621
ACS Nano 2019, 13, 8926−8935

(33) Bhaviripudi, S.; Jia, X.; Dresselhaus, M. S.; Kong, J. Role of Kinetic Factors in Chemical Vapor Deposition Synthesis of Uniform Large Area Graphene Using Copper Catalyst. *Nano Lett.* **2010**, *10*, 4128−4133.
(34) Yan, Z.; Lin, J.; Peng, Z.; Sun, Z.; Zhu, Y.; Li, L.; Xiang, C.; Samuel, E. L.; Kittrell, C.; Tour, J. M. Toward the Synthesis of Wafer-Scale Single-Crystal Graphene on Copper Foils. *ACS Nano* **2012**, *6*, 9110−9117.
(35) Wang, H.; Wang, G.; Bao, P.; Yang, S.; Zhu, W.; Xie, X.; Zhang, W.-J. Controllable Synthesis of Submillimeter Single-Crystal Monolayer Graphene Domains on Copper Foils by Suppressing Nucleation. *J. Am. Chem. Soc.* **2012**, *134*, 3627−3630.
(36) Bonaccorso, F.; Lombardo, A.; Hasan, T.; Sun, Z. P.; Colombo, L.; Ferrari, A. C. Production and Processing of Graphene and 2d Crystals. *Mater. Today* **2012**, *15*, 564−589.
(37) Yu, Q.; Lian, J.; Siriponglert, S.; Li, H.; Chen, Y. P.; Pei, S.-S. Graphene Segregated on Ni Surfaces and Transferred to Insulators. *Appl. Phys. Lett.* **2008**, *93*, 113103.
(38) Wang, Y.; Zheng, Y.; Xu, X. F.; Dubuisson, E.; Bao, Q. L.; Lu, J.; Loh, K. P. Electrochemical Delamination of CVD-Grown Graphene Film: Toward the Recyclable Use of Copper Catalyst. *ACS Nano* **2011**, *5*, 9927−9933.
(39) Gannett, W.; Regan, W.; Watanabe, K.; Taniguchi, T.; Crommie, M. F.; Zettl, A. Boron Nitride Substrates for High Mobility Chemical Vapor Deposited Graphene. *Appl. Phys. Lett.* **2011**, *98*, 242105.
(40) Petrone, N.; Dean, C. R.; Meric, I.; van der Zande, A. M.; Huang, P. Y.; Wang, L.; Muller, D.; Shepard, K. L.; Hone, J. Chemical Vapor Deposition-Derived Graphene with Electrical Performance of Exfoliated Graphene. *Nano Lett.* **2012**, *12*, 2751−2756.
(41) Calado, V. E.; Zhu, S. E.; Goswami, S.; Xu, Q.; Watanabe, K.; Taniguchi, T.; Janssen, G. C. A. M.; Vandersypen, L. M. K. Ballistic Transport in Graphene Grown by Chemical Vapor Deposition. *Appl. Phys. Lett.* **2014**, *104*, 023103.
(42) Wang, R.; Whelan, P. R.; Braeuninger-Weimer, P.; Tappertzhofen, S.; Alexander-Webber, J. A.; Van Veldhoven, Z. A.; Kidambi, P. R.; Jessen, B. S.; Booth, T.; Bøggild, P.; Hofmann, S. Catalyst Interface Engineering for Improved 2d Film Lift-Off and Transfer. *ACS Appl. Mater. Interfaces* **2016**, *8*, 33072−33082.
(43) Banszerus, L.; Schmitz, M.; Engels, S.; Dauber, J.; Oellers, M.; Haupt, F.; Watanabe, K.; Taniguchi, T.; Beschoten, B.; Stampfer, C. Ultrahigh-Mobility Graphene Devices from Chemical Vapor Deposition on Reusable Copper. *Sci. Adv.* **2015**, *1*, No. e1500222.
(44) Banszerus, L.; Schmitz, M.; Engels, S.; Goldsche, M.; Watanabe, K.; Taniguchi, T.; Beschoten, B.; Stampfer, C. Ballistic Transport Exceeding 28μm in CVD Grown Graphene. *Nano Lett.* **2016**, *16*, 1387−1391.
(45) Drögeler, M.; Banszerus, L.; Volmer, F.; Taniguchi, T.; Watanabe, K.; Beschoten, B.; Stampfer, C. Dry-Transferred CVD Graphene for Inverted Spin Valve Devices. *Appl. Phys. Lett.* **2017**, *111*, 152402.
(46) Chen, S.; Brown, L.; Levendorf, M.; Cai, W.; Ju, S.-Y.; Edgeworth, J.; Li, X.; Magnuson, C. W.; Velamakanni, A.; Piner, R. D.; Kang, J.; Park, J.; Ruoff, R. S. Oxidation Resistance of Graphene-Coated Cu and Cu/Ni Alloy. *ACS Nano* **2011**, *5*, 1321−1327.
(47) Wang, M.; Jang, S. K.; Jang, W.-J.; Kim, M.; Park, S.-Y.; Kim, S.-W.; Kahng, S.-J.; Choi, J.-Y.; Ruoff, R. S.; Song, Y. J.; Lee, S. A Platform for Large-Scale Graphene Electronics − CVD Growth of Single-Layer Graphene on CVD-Grown Hexagonal Boron Nitride. *Adv. Mater.* **2013**, *25*, 2746−2752.
(48) Shautsova, V.; Gilbertson, A. M.; Black, N. C. G.; Maier, S. A.; Cohen, L. F. Hexagonal Boron Nitride Assisted Transfer and Encapsulation of Large Area CVD Graphene. *Sci. Rep.* **2016**, *6*, 30210.
(49) Braeuninger-Weimer, P.; Brennan, B.; Pollard, A. J.; Hofmann, S. Understanding and Controlling Cu-Catalyzed Graphene Nucleation: The Role of Impurities, Roughness, and Oxygen Scavenging. *Chem. Mater.* **2016**, *28*, 8905−8915.
(50) Taniguchi, T.; Watanabe, K. Synthesis of High-Purity Boron Nitride Single Crystals under High Pressure by Using Ba-Bn Solvent. *J. Cryst. Growth* **2007**, *303*, 525−529.
(51) Dean, C. R.; Young, A. F.; Meric, I.; Lee, C.; Wang, L.; Sorgenfrei, S.; Watanabe, K.; Taniguchi, T.; Kim, P.; Shepard, K. L.; Hone, J. Boron Nitride Substrates for High-Quality Graphene Electronics. *Nat. Nanotechnol.* **2010**, *5*, 722−726.
(52) Kretinin, A. V.; Cao, Y.; Tu, J. S.; Yu, G. L.; Jalil, R.; Novoselov, K. S.; Haigh, S. J.; Gholinia, A.; Mishchenko, A.; Lozada, M.; Georgiou, T.; Woods, C. R.; Withers, F.; Blake, P.; Eda, G.; Wirsig, A.; Hucho, C.; Watanabe, K.; Taniguchi, T.; Geim, A. K.; et al. Electronic Properties of Graphene Encapsulated with Different Two-Dimensional Atomic Crystals. *Nano Lett.* **2014**, *14*, 3270−3276.
(53) Pizzocchero, F.; Gammelgaard, L.; Jessen, B. S.; Caridad, J. M.; Wang, L.; Hone, J.; Bøggild, P.; Booth, T. J. The Hot Pick-up Technique for Batch Assembly of Van Der Waals Heterostructures. *Nat. Commun.* **2016**, *7*, 11894.
(54) Lagatsky, A. A.; Sun, Z.; Kulmala, T. S.; Sundaram, R. S.; Milana, S.; Torrisi, F.; Antipov, O. L.; Lee, Y.; Ahn, J. H.; Brown, C. T. A.; Sibbett, W.; Ferrari, A. C. 2μm Solid-State Laser Mode-Locked by Single-Layer Graphene. *Appl. Phys. Lett.* **2013**, *102*, 013113.
(55) Ferrari, A. C.; Meyer, J. C.; Scardaci, V.; Casiraghi, C.; Lazzeri, M.; Mauri, F.; Piscanec, S.; Jiang, D.; Novoselov, K. S.; Roth, S.; Geim, A. K. Raman Spectrum of Graphene and Graphene Layers. *Phys. Rev. Lett.* **2006**, *97*, 187401.
(56) Ferrari, A. C.; Basko, D. M. Raman Spectroscopy as a Versatile Tool for Studying the Properties of Graphene. *Nat. Nanotechnol.* **2013**, *8*, 235−246.
(57) Cancado, L. G.; Jorio, A.; Ferreira, E. H.; Stavale, F.; Achete, C. A.; Capaz, R. B.; Moutinho, M. V.; Lombardo, A.; Kulmala, T. S.; Ferrari, A. C. Quantifying Defects in Graphene *Via* Raman Spectroscopy at Different Excitation Energies. *Nano Lett.* **2011**, *11*, 3190−3196.
(58) Das, A.; Pisana, S.; Chakraborty, B.; Piscanec, S.; Saha, S. K.; Waghmare, U. V.; Novoselov, K. S.; Krishnamurthy, H. R.; Geim, A. K.; Ferrari, A. C.; Sood, A. K. Monitoring Dopants by Raman Scattering in an Electrochemically Top-Gated Graphene Transistor. *Nat. Nanotechnol.* **2008**, *3*, 210−215.
(59) Basko, D. M.; Piscanec, S.; Ferrari, A. C. Electron-Electron Interactions and Doping Dependence of the Two-Phonon Raman Intensity in Graphene. *Phys. Rev. B: Condens. Matter Mater. Phys.* **2009**, *80*, 165413.
(60) Arenal, R.; Ferrari, A. C.; Reich, S.; Wirtz, L.; Mevellec, J. Y.; Lefrant, S.; Rubio, A.; Loiseau, A. Raman Spectroscopy of Single-Wall Boron Nitride Nanotubes. *Nano Lett.* **2006**, *6*, 1812−1816.
(61) Reich, S.; Ferrari, A. C.; Arenal, R.; Loiseau, A.; Bello, I.; Robertson, J. Resonant Raman Scattering in Cubic and Hexagonal Boron Nitride. *Phys. Rev. B: Condens. Matter Mater. Phys.* **2005**, *71*, 205201.
(62) Nemanich, R. J.; Solin, S. A.; Martin, R. M. Light Scattering Study of Boron Nitride Microcrystals. *Phys. Rev. B: Condens. Matter Mater. Phys.* **1981**, *23*, 6348−6356.
(63) Mohiuddin, T. M. G.; Lombardo, A.; Nair, R. R.; Bonetti, A.; Savini, G.; Jalil, R.; Bonini, N.; Basko, D. M.; Galiotis, C.; Marzari, N.; Novoselov, K. S.; Geim, A. K.; Ferrari, A. C. Uniaxial Strain in Graphene by Raman Spectroscopy: G Peak Splitting, Gruneisen Parameters, and Sample Orientation. *Phys. Rev. B: Condens. Matter Mater. Phys.* **2009**, *79*, 205433.
(64) Proctor, J. E.; Gregoryanz, E.; Novoselov, K. S.; Lotya, M.; Coleman, J. N.; Halsall, M. P. High-Pressure Raman Spectroscopy of Graphene. *Phys. Rev. B: Condens. Matter Mater. Phys.* **2009**, *80*, 073408.
(65) Zabel, J.; Nair, R. R.; Ott, A.; Georgiou, T.; Geim, A. K.; Novoselov, K. S.; Casiraghi, C. Raman Spectroscopy of Graphene and Bilayer under Biaxial Strain: Bubbles and Balloons. *Nano Lett.* **2012**, *12*, 617−621.
(66) Yoon, D.; Son, Y.-W.; Cheong, H. Strain-Dependent Splitting of the Double-Resonance Raman Scattering Band in Graphene. *Phys. Rev. Lett.* **2011**, *106*, 155502.
(67) Lee, J. E.; Ahn, G.; Shim, J.; Lee, Y. S.; Ryu, S. Optical Separation of Mechanical Strain from Charge Doping in Graphene. *Nat. Commun.* **2012**, *3*, 1024.

DOI: 10.1021/acsnano.9b02621
ACS Nano 2019, 13, 8926−8935

(68) Piscanec, S.; Lazzeri, M.; Mauri, F.; Ferrari, A. C.; Robertson, J. Kohn Anomalies and Electron-Phonon Interactions in Graphite. *Phys. Rev. Lett.* **2004**, *93*, 185503.
(69) Novoselov, K. S.; Geim, A. K.; Morozov, S. V.; Jiang, D.; Zhang, Y.; Dubonos, S. V.; Grigorieva, I. V.; Firsov, A. A. Electric Field Effect in Atomically Thin Carbon Films. *Science* **2004**, *306*, 666−669.
(70) Kim, K. K.; Hsu, A.; Jia, X.; Kim, S. M.; Shi, Y.; Dresselhaus, M.; Palacios, T.; Kong, J. Synthesis and Characterization of Hexagonal Boron Nitride Film as a Dielectric Layer for Graphene Devices. *ACS Nano* **2012**, *6*, 8583−8590.
(71) Xia, J.; Chen, F.; Li, J.; Tao, N. Measurement of the Quantum Capacitance of Graphene. *Nat. Nanotechnol.* **2009**, *4*, 505−509.
(72) Couto, N. J. G.; Costanzo, D.; Engels, S.; Ki, D. K.; Watanabe, K.; Taniguchi, T.; Stampfer, C.; Guinea, F.; Morpurgo, A. F. Random Strain Fluctuations as Dominant Disorder Source for High-Quality on-Substrate Graphene Devices. *Phys. Rev. X* **2014**, *4*, 041019.
(73) Hwang, E. H.; Adam, S.; Das Sarma, S. Carrier Transport in Two-Dimensional Graphene Layers. *Phys. Rev. Lett.* **2007**, *98*, 186806.
(74) Van der Pauw, L. J. A Method of Measuring Specific Resistivity and Hall Effect of Discs of Arbitrary Shape. *Philips Res. Rep.* **1958**, *13*, 1−9.
(75) Hwang, E. H.; Das Sarma, S. Acoustic Phonon Scattering Limited Carrier Mobility in Two-Dimensional Extrinsic Graphene. *Phys. Rev. B: Condens. Matter Mater. Phys.* **2008**, *77*, 115449.
(76) Blake, P.; Yang, R.; Morozov, S. V.; Schedin, F.; Ponomarenko, L. A.; Zhukov, A. A.; Nair, R. R.; Grigorieva, I. V.; Novoselov, K. S.; Geim, A. K. Influence of Metal Contacts and Charge Inhomogeneity on Transport Properties of Graphene near the Neutrality Point. *Solid State Commun.* **2009**, *149*, 1068−1071.

DOI: 10.1021/acsnano.9b02621
ACS Nano 2019, 13, 8926−8935